

Chapter 1 Muon Beamline

1.1 Introduction

In this chapter, we discuss the muon beamline. This includes the collimators and anti-proton stopping window in the Transport Solenoid (TS), and the muon stopping target, beam monitor, proton and neutron absorbers, beam stop, vacuum system and support structures in the Detector Solenoid (DS) region. The TS system filters the particle flux producing a momentum- ($< 0.08 \text{ GeV}/c$) and charge-selected muon beam, with good reduction in contamination from e^\pm , μ^\pm , π^\pm , p , and \bar{p} during the detector live-time. The muons have high efficiency for stopping in the muon stopping target, and the electron momentum spectrum from muon decay in flight cuts off well below the electron momentum from $\mu - e$ conversion, $105.0 \text{ MeV}/c$ in Aluminum and $104.3 \text{ MeV}/c$ in Titanium. A germanium crystal x ray detector measures the absolute rate for muonic atom formation, and functions as a continuous real-time muon beam monitor. Muons not stopped in the target are transported to the muon beam-stop. Protons and neutrons originating from muon capture in the stopping target are attenuated by absorbers to minimize detector background rates. Finally, detector support and vacuum requirements are discussed.

1.2 Collimators

The design of the transport solenoid is discussed at length in Chapter 7. The purpose of the collimators is to exploit the slow drift, perpendicular to the plane of the S-shaped TS magnet, in opposite directions by positive and negative charges. The vertical displacement midway through the S-shape TS magnet is:

$$D(m) = -\frac{Q}{e} \frac{\pi}{0.6B(T)} \frac{P_L^2 + 0.5P_T^2}{P_L (\text{GeV}/c)}$$

where e is the charge of the electron, and P_L (P_T) is along (transverse) the magnetic field. Besides this slow drift, the particles execute fast gyrations with radius:

$$a(m) = \frac{P_T (\text{GeV}/c)}{0.3B(T)}$$

As can be seen from the above equations, the collimators filter the beam favoring low-momentum particles. The anti-protons are highly non-relativistic, and stop in the 0.007 inch thick Kapton anti-proton stopping window. Almost all the electrons are relativistic and largely pass before the start of the detector live-time, which begins about 650ns after the proton bunch hits the target. The pions largely decay before the start of the detector live-time. All positively charged particles and high momentum particles are highly attenuated by the collimators.

Cylindrical collimators are placed in the first and last straight sections of the TS. The first collimator is made of cooper. The last is made of polyethylene (CH_2) loaded with either Boron or Lithium to protect the detectors from neutron backgrounds. The important dimensions are given in Table 1. The mid-TS collimator passes muons with $1 < z < -19 \text{ cm}$. Recently, thin annular foils with inner radius 8.5 cm were

added to collimator 3 to stop low energy muons which would miss the muon stopping target, and shielding was added to protect the TS coils from radiation from the proton target (see MECO WBS 1.5.2 Reference Design). The first two collimators with the TS shielding are shown in Figure 1.1.

Table 1: Parameters of three TS collimators from WBS 1.5.2 Reference Design. Position of the center is in the standard MECO coordinate system. The central collimator also restricts $1 < z < -19\text{cm}$, as shown in Figure 1.1.

Collimator	Position of Center	Inner Radius	Length
1	390.4, 0, -345.4 cm	15-17 cm	1 m
2	0, -9, 0 cm	15 cm	0.8 m
3	-390.4, 0, 343 cm	12.8 cm	1 m

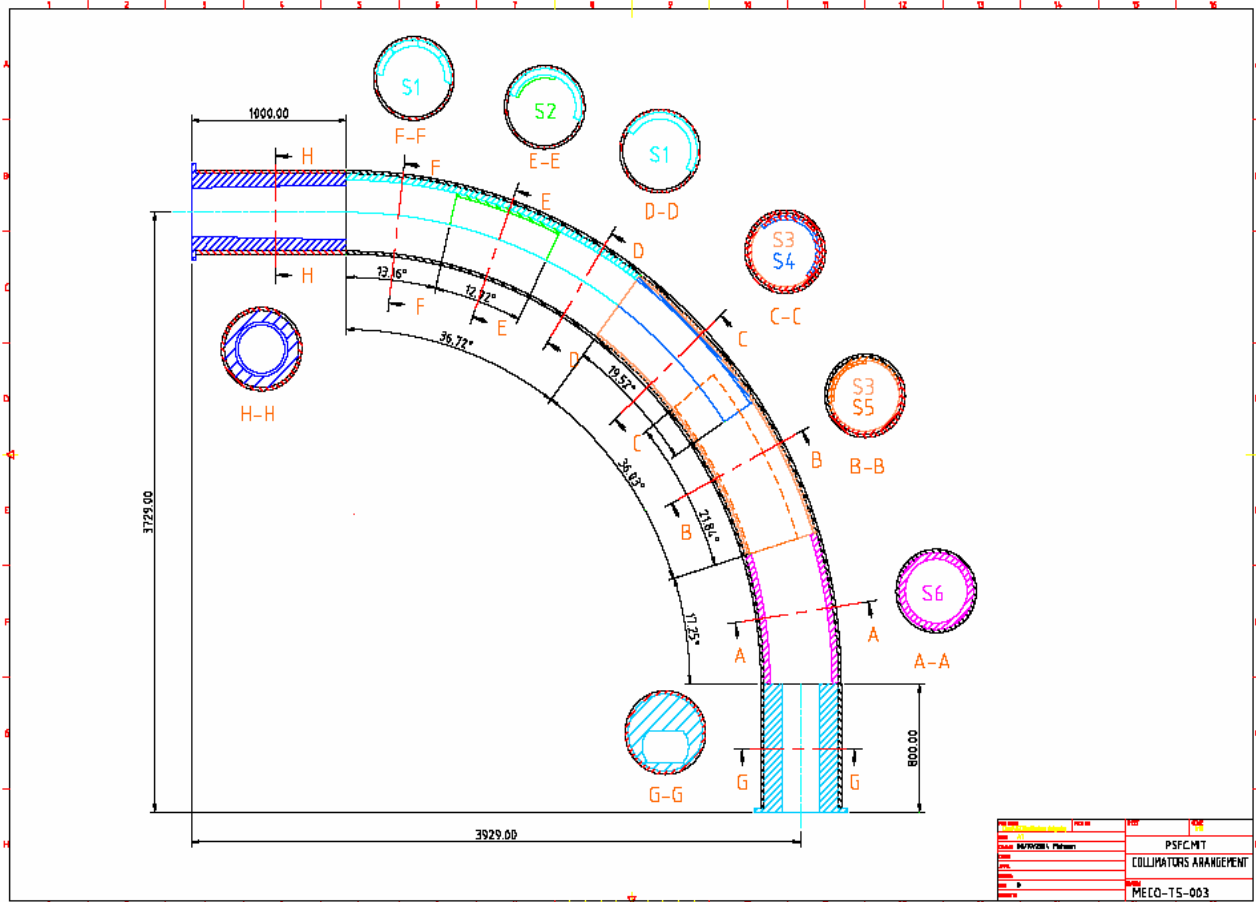


Figure 1.1 Conceptual engineering drawing {mec0 110} showing the first and second collimators (H and G), and the shielding to protect the TS coils (S).

Collimator sizes were optimized to remove or heavily suppress electrons above 100 MeV, a potential source of background. GEANT simulation studies using the collimators described above in a full simulation of MECO with 10^7 primary protons on the production target completely eliminated 100 MeV electrons at the exit to the TS. Furthermore, by design of the graded magnetic field, 100 MeV electrons originating in the production solenoid will have insufficient P_T to hit the detectors.

1.3 Absorbers

The MECO absorbers in the Detector Solenoid area are designed to moderate protons and neutrons. Figure 1.2 shows a schematic view of the DS magnet, revealing the boron or lithium loaded polyethylene proton absorber and neutron absorbers inside the DS vacuum. The largest potential contribution to the tracking detector rate is from protons from muon capture in the stopping target. Without shielding, the average rate in individual tracking detector elements is above 10^6 Hz. However, the average rate from protons is reduced to 10^5 Hz with the proton shield {meco100}. The interface between the neutron absorbing shielding material and the DS is as follows:

- Individual pieces of the shielding material will rest against the walls of the DS warm bore. These pieces have an axially varying weight load as high as 23.6 kg/cm at the upstream end to 6.34 kg/cm at the downstream end of the magnet.
- The shielding material will bolt to the threaded bars welded to the warm bore walls, as described in the *Conceptual Design of the MECO DS Warm Bore Attachments* document on the MECO web page.

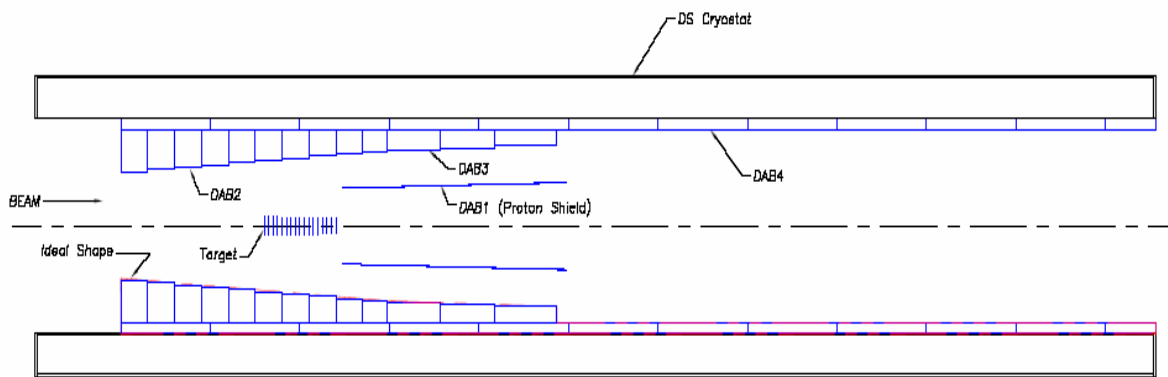


Figure 1.2: Schematic drawing of the Proton and Neutron Shields in the Detector Solenoid. DAB1 represents the proton shield. DAB2-4 represent different sections of the neutron shield.

Neutrons produced in the muon stopping target are a potential source of background in the cosmic ray veto counters that surround the Detector Solenoid. The MARS {meco128} Monte-Carlo program was used to simulate these neutrons. Although these studies are continuing, acceptable fluxes were obtained with 30% boron loaded polyethylene. Lithium loaded polyethylene was also studied, but it is more expensive and did not significantly reduce the flux in the detectors.

1.4 Stopping Target

The goal of the stopping target design is to maximize the probability for beam muons to stop and for conversion electrons to be detected in the tracker and calorimeter. At the same time, the target should be designed to minimize the energy loss of conversion electrons as they exit the target and to minimize the number of electrons from muon DIO that reach the tracking detector. Furthermore, detector rates, e.g. beam electron bremsstrahlung, and backgrounds, e.g. cosmic ray interactions in the target, are minimized with the smallest possible target mass. The transverse size, thickness, spacing, and number of thin disks that comprise the target were optimized to best achieve these goals.

The baseline target, with mass 159 g, has seventeen 0.02 cm thick Aluminum disks. They are arranged parallel to each other, centered on the Solenoid Magnet axis and with each face perpendicular to it. The

target is tapered in the downstream direction, with 5.0 cm disk spacing and radii from 8.30 cm to 6.53 cm. The target is placed in the graded portion of the DS magnetic field, with the first disk at 1.57 T and the last at 1.30 T.

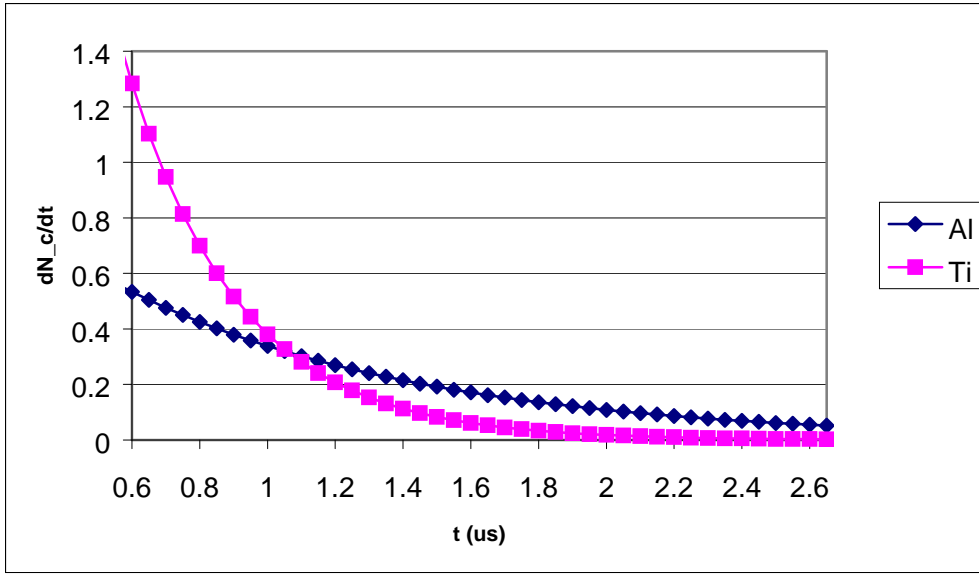
Muons stopped in the target supports produce decay electrons with much larger detector acceptances than those which stop in the target. This requires the target support mass to be kept to a minimum. A design study for target support and of the consequent detector rates is planned. A simplified calculation of the detector rate from the support material follows. The figure of merit for the support material is the ratio of tensile strength T to density ρ ; for this preliminary study we use Aluminum alloy 360 with $T = 325$ Mpa and $\rho = 2.64$ g/cm³. The ratio of the mass of the support inside the muon beam profile to the mass of the target, supported at the tensile strength, is $R = \rho L g / T = 10^{-5}$. It is convenient to take this equal to the ratio of the number of muons which stop in the target supports compared to stopping in the target. The diameter of the support wire is typically 20 μ m. A simplified calculation of the detector acceptance for muon decays originating in the supports compared to the target gives 10^4 . Thus, the ratio of the flux of DIO electrons hitting the detectors coming from the supports to that from the target is roughly estimated to be 10^{-1} . The fraction of the detector rates from muon decays are ~ 0.2 ; hence, 2% of the total rate. This would be acceptable, however, careful design studies are needed.

We are also planning to use a Titanium target. There has not been a conceptual design of the Titanium target yet. The μ^- lifetime in Titanium is much shorter than in Aluminum (see Table 2) leading to almost twice the maximum capture rate at the beginning of the detector live-time (see Figure 1.3). The tracker rates are dominated by capture secondaries. However, the predicted Titanium muon conversion BR varies from 1.5 to 1.7 times that of Aluminum, depending on whether the new physics process is scalar or vector in form {Kitano:2002}. Also Titanium has a shorter radiation length relative to the dE/dx stopping power, leading to increased backgrounds. At this point, given the simulations performed thus far, it is not possible to say which target will give the best signal/background. At the February, 2005 UCI MECO meeting, the collaboration decided that we should build both.

Table 2: Comparison of Aluminum and Titanium targets.

Target	Al	Ti
μ^- Lifetime	880 ns	329 ns
f_{cap} vs f_{DIO}	60% vs 40%	85% vs 15%
Conversion BR Ti/Al	1.0	$\approx 1.5 - 1.7$
dE/dx (min)	1.62 MeV cm ² /g	1.48 MeV cm ² /g
X_0	24.0 g/cm ²	16.2 g/cm ²

Figure 1.3: Relative rate of muon captures for Aluminum and Titanium targets.



1.5 Muon Target Monitor

1.5.1 Purpose and Method

Given the complexity of generating and collecting low energy negative muons in the production solenoid, and transporting them via the transport solenoid to the target foils in the detector solenoid, it is evident that some means of confirming the rate and integral number of negative muons which stop on the target foils is crucial. It is equally evident that such a device will prove indispensable in the initial process of tuning conditions for the proton beam and the solenoids.

We propose that an effective and reliable Muon Stopping Target Monitor can be established by observing the prompt production of muonic x-rays which signal the formation of muonic atoms in the target foils. This objective can be achieved if it is possible to conveniently locate a germanium detector where it can view, without serious deadtime, photons coming from the target foils. Such x-rays are unambiguously characteristic of a muonic atom's atomic number Z . In addition, the highest yield x-ray is the $2p \rightarrow 1s$ radiative transition which confirms the arrival of a muon in the initial state needed for $\mu-e$ conversion. Other observable x-rays, having substantial yields and signaling arrival in the $1s$ state, are the $3p \rightarrow 1s$, and the $4p \rightarrow 1s$. Typically the $3d \rightarrow 2p$ transition which populates the $2p$ state also appears in the energy spectrum. The study of such exotic atom x-rays has a long and productive history which closely parallels the development of semiconductor spectrometers, the Si(Li) for detecting low photon energies and the intrinsic Ge for medium-to-high energies. Members of this Collaboration have had extensive experience in these fields.

Table 3: Transition energies for muonic atoms: Aluminum and Titanium

Transition	Al (keV)	Ti (keV)
3d - 2s	66	189
2p - 1s	356	1021
3p - 1s	423	1210

A germanium detector crystal of significant size should be used to collect the energy spectrum of the muonic x-rays whether the target foils be Aluminum or Titanium. Table 3 lists approximate energies for x-rays from Al and Ti. Recording the rate of these full energy photons at a FWHM resolution of 2.2 keV unambiguously identifies and monitors negative muons arriving in the 1s atomic level of the stopping target material.

In principle, this detector is also sensitive to the possible generation of pionic or antiprotonic x-rays if these negative particles were to reach the target foils. However, observable x-ray energies from these hadronic atom transitions are cut off when the radiative rate from a given upper atomic level is overtaken by the competing strong nuclear absorption rate. This coupled with the short lifetime of 26 ns for pions should rule out a pionic target-atom signal. On the other hand a beam contamination of antiprotons stopping on the Aluminum foils might have a measurable yield for the circular $4f \rightarrow 3d$ x-ray, 202 keV in Al or 588 keV in Ti, and possibly the $3d \rightarrow 2p$, 586 keV in Al or 1679 keV in Ti.

1.5.2 Location for the Germanium Detector

Three requirements determine the best location for the Ge detector to view the muon target:

1. The detector should only view the target, if possible. Hence the first requirement is for good collimation ahead of the detector.
2. Because of the extraordinarily high x-ray rate, about 10^{11} Hz, the detector must be far from the source, along a low-attenuation path, and
3. The detector must be lie beyond the DS magnetic field where it can be serviced periodically with cryogenic liquid and annealed to repair neutron damage.

Figure 1.4 shows an optimal layout for the Ge detector which satisfies these requirements. The photon spectrometer is placed along the axis of the detector solenoid, at the downstream end of the moveable concrete shield wall. From there it views all foils head-on, with the front foil 15 m and the downstream foil 14 m away. Collimation is conveniently provided by bore holes in the 0.5 m steel wall and the 1.0 m concrete wall. A sectioned vacuum pipe runs through these walls starting at the back face of the detector solenoid. The pipe is not coupled to the detector solenoid so that the section through the steel wall can travel with the wall whenever it is necessary to gain access to the detector solenoid.

Figure 1.4: Layout of Muon Beam Monitor

Figure 1.5: Europium-152 Calibration Lines listed in keV

Transmission of 356 keV x-rays passing through all 17 Aluminum foils is 90%. At the back end of the DS vessel a 5 cm dia. stainless window of 0.2 cm thickness and thin windows on the vacuum pipe transmit 85% at this photon energy. For muons stopping in the steel window the muonic x-ray energy is $E(2p \rightarrow 1s) = 1426$ keV. Beyond the DS vessel a vacuum pipe transports photons through the stainless steel wall and the heavy shielding block wall to the photon spectrometer endcap. Copper ring collimators placed within the vacuum pipe limit photons to the central 3 cm dia. portion of the germanium crystal, defining a target center-to-crystal fractional solid angle of 3.1×10^{-7} . At a muon

stopping rate of 10^{11} Hz the germanium detector will process the K-series x-ray events ($2p \rightarrow 1s$, $3p \rightarrow 1s$, $4p \rightarrow 1s$) at 31 kHz. A 45 cm^3 germanium crystal with 3 cm depth is expected to capture full-energy events for the 356 keV x-ray of muonic Aluminum with an efficiency of about 50%. For the 1021 keV x-ray of muonic Titanium this efficiency drops to 33%. The combination of high, full-energy event efficiency and excellent peak resolution (2.2 keV) assures that the muonic atom formation process is well determined.

1.5.3 Calibration

The spectrometer system can be calibrated in the standard way, which typically involves one or more calibrated radioisotopes. It happens in our case that a single source of Europium- 152 (12.7 year half-life) spans the energy range of muonic x-rays for either an Aluminum or a Titanium target. A $10 \mu\text{Ci}$ strength source placed just outside the detector endcap can accomplish this. Typically calibration data is collected simultaneously with the experimental data if the muonic lines are not overlapped by calibration lines. The well established gamma energies and experimental yields for ^{152}Eu are illustrated in the semilog plot of Figure 1.5.

To obtain an absolute measurement of the muonic atom formation rate it is necessary to make an absolute calibration of the total efficiency (detector energy efficiency \times solid angle) for gammas leaving the target position and being detected by the germanium detector. For this a special measurement of the total efficiency can be made anywhere once the Ge detector system is available. A stronger ^{152}Eu source ($100 \mu\text{Ci}$) can be used in a full scale mockup of target foils, Ge detector, windows, collimators, and vacuum or helium environment. Locating the source at various target foil positions, spectra can be taken over long time-interval runs to map out the total efficiency.

1.5.4 Selection of Germanium Spectrometer System

A number of vendors supply complete spectrometer systems. Three prominent vendors are Princeton Gamma Tech(PGT), Perkin-Elmer (Ortec) and Canberra. At the present time we have a quotation from PGT, and have requested the same from the other two forms.

Among our early concerns about viewing in this location the target with such a system were the following:

1. The event rate in the detector for muonic x-rays originating in the target foils is quite high when compared to previous muonic x-ray experiments :

With today's high rate preamplifiers of the transistor-reset variety this is no longer a problem. These are rated as capable of maintaining a fwhm resolution of 2.2 keV while handling a count rate of 800,000 MeV per sec. This should readily satisfy our requirements.

2. The detector rate for the interaction of fast muon-capture neutrons ($> 0.5 \text{ MeV}$) is high enough to induce damage in the detector's germanium crystal :

This stems from the fact that fast neutrons can cause nuclear dislocations in the crystal lattice thereby building up trapping centers for the signal charge carriers. At a level of 10^9 dislocations

per cm^2 in n-type germanium a deterioration of peak shape resolution will begin to show in terms of a low energy tail. The nuclear interaction length in germanium is 88.3 g/cm^2 . Therefore in a 3 cm thick crystal 17% of the neutrons can interact. Given that half of the muons capture on Aluminum, producing fast neutrons, this leads to a rate for inelastic neutron events in the Ge crystal of 2.6 kHz. In a 10^7 sec run there will be a need to rehabilitate the crystal every 1-to-1.5 months. Should damage become evident it is possible to anneal the crystal off-line using the vendor's neutron radiation repair kit. For n-type germanium the charge carriers are electrons. When trapped in a lattice defect these can be released quickly with less serious reduction in the total collected charge than for p-type germanium. Hence we would select an n-type intrinsic germanium detector with a fast-reset preamplifier for best high-rate performance. The need to periodically anneal the detector for damage could take this system down for possibly a shift or two. For this reason we believe there is a need for a backup detector in the Target Monitoring system.

3. The transport solenoid delivers a flux of electrons to the detector solenoid which is about 500 times greater than that for negative muons in the initial 150 ns following a proton pulse. In the interval between 150-to-750 ns, when most of the muons arrive, this ratio falls toward 1.0. These electrons have energies ranging up to 70 MeV. Bremsstrahlung photons are produced in the forward direction by 16% of the electrons passing through the target foils. These photons, therefore, add to the muonic x-ray flux arriving at the germanium detector :

Beam electrons are to be swept from the vacuum pipe by applying a transverse field of 0.1 T across the pipe. This would provide a deflection sufficient to remove the electrons from the pipe within a field length of less than one meter. The best location for this sweeper would be between the stainless steel wall and the back concrete block. Bremsstrahlung photons would be dealt with by inhibiting the preamplifier during the 0-to-150 ns interval.

1.6 Beam Stop

The muon beam stop (MBS) is designed to absorb the energy of beam particles, which consist mainly of e^- and μ^- (see Table 8.3) that reach the end of the detector solenoid, while minimizing the background to the detectors from the muon decays and captures in the beam stop, especially during the detector live-time, which begins about 650ns after the proton bunch hits the target {meco127}. Of the beam particles that arrive at the stopping target region, 50% of muons and 84% of electrons continue towards the dump. Bremsstrahlung photons produced by electrons, and the products of muon decay and capture in the beam stop can hit the detectors if the beam stop is placed too close. Near the rear of the detector solenoid the axial magnetic field intensity drops along the beam stop direction; this is a critical feature of the beam stop. The field gradient reflects most charged particles produced in the stop away from the detectors.

During the beam stop optimization we satisfied the following requirements: the beam stop should be far from the detectors and the solid angle from the beam stop to the detectors should be minimized to reduce the flux of secondary particles leaving the beam stop in the direction of the tracker and calorimeter. The inner radius of the beam stop cylinder walls can not be too small, otherwise the muons and decay in flight electrons start to hit the walls earlier in the region close to the calorimeter. This defines a requirement that the first part of the beam stop should have the inner radius only somewhat smaller than the minimal distance from the calorimeter to the axis. The second part of the beam stop should have a small radius, but at the same time allow all electrons and muons to propagate to the downstream face of the beam stop. We have chosen the radius of the second part of the beam stop $R=32 \text{ cm}$ and the position

of the downstream face of the beam stop $z = 1700\text{cm}$, in the standard MECO coordinate system. One can see in Figure 1.6 and Figure 1.7 that in this case all the late electrons (arrival time after 600ns) and muons hit the walls of the beam stop in the region $z > 1600\text{cm}$. In this region the field is less than 0.05 T (5% of the 1.0 T magnetic field in the tracker region). Almost all the beam particles hit the downstream face of the beam stop.

Table 8.3: Particles flux per beam proton at the Detector solenoid entrance from FLUKA simulations. “Late” particles have an arrival time after 600 ns.

	All μ^-	All μ^+	All e^-	Late e^-	All e^+	Late e^+	All π^-
Flux	1.8×10^{-2}	8.2×10^{-6}	0.226	4.6×10^{-4}	0.0324	7.4×10^{-5}	2.7×10^{-6}

To make a choice of the material to be used on the inner surface of the beam stop, the following considerations were taken into account. There are some benefits to a high atomic number material on the inner surface of the beam stop, as almost all muons are quickly captured; the muon lifetime in the Lead, for example, is only 80ns. Therefore, the secondary particles from the beam stop do not contribute to the detector and calorimeter rates during the measurement period. Unfortunately, the neutrons from the muon capture cause unacceptable radiation damage of APDs in the calorimeter. The calculated neutron flux in the calorimeter region from the muon capture in the beam stop is shown in Table 4. The neutron flux in the calorimeter from the CH_2 beam stop is less than the neutron flux from muon capture in the Aluminum stopping target, 3×10^{10} neutrons/ cm^2 over the life of the experiment, whereas the Lead beam stop gives considerably more neutron flux in the calorimeter. The need to limit the APD radiation damage from neutrons led to our choice of CH_2 for inner surface of the beam stop.

Table 4 Peak neutron flux in the calorimeter from muon capture in the beam stop during the life of the experiment (10^7 sec).

Material on the inner surface of the beam stop	Peak neutron flux in the calorimeter, n/ cm^2
Lead	4×10^{11}
CH_2	6×10^9

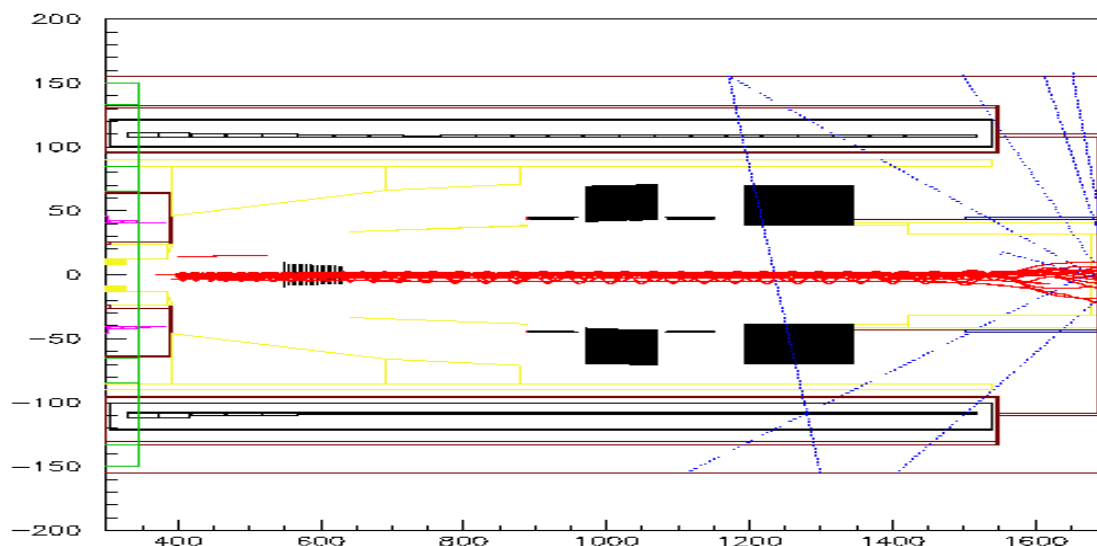


Figure 1.6 Trajectories of beam electrons with late arrival time (after 600 ns). In this plot, the electron trajectories start at the end of the TS. Red indicates electrons, blue indicates gammas.

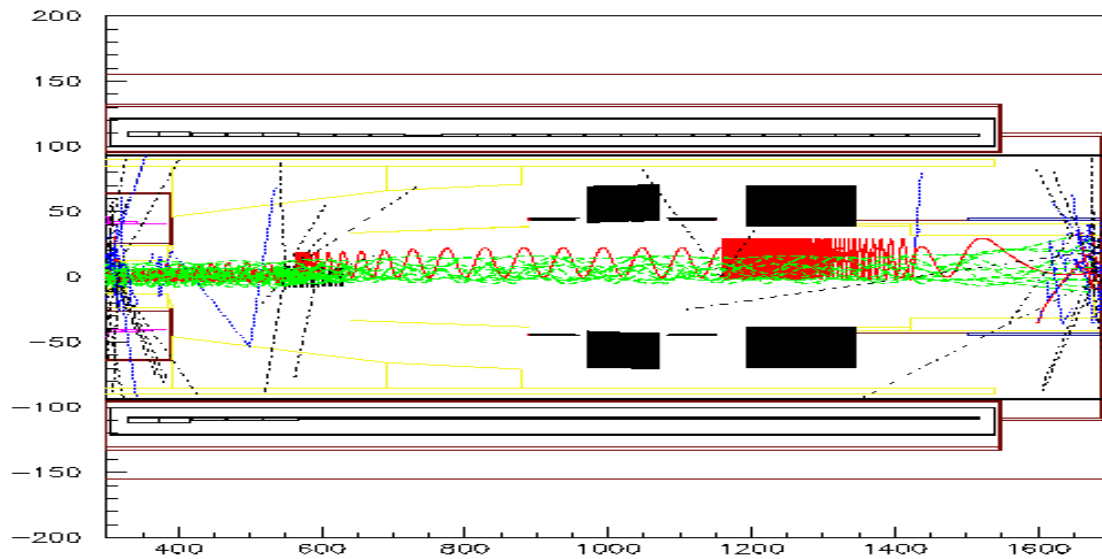


Figure 1.7 Trajectories of beam muons (green) and electrons (red) from muon decays. Blue indicates gammas, dashed black lines indicates neutrons. CH₂ is indicated by yellow lines.

Finally the beam stop has a 2cm thick stainless steel cylinder which covers the whole region between the calorimeter and the front face of vacuum closure cap (see Figure 1.8). From the inner surface it is covered by CH₂, with 2 cm thickness on the first 75 cm along the z axis and 9 cm thickness on the remaining 268 cm. To decrease the flux of bremsstrahlung photons at the vacuum pump locations, the beam stop stainless steel cylinder is covered from outside by a 2 cm thick Lead layer, which is 184cm in length. The cosmic ray shield inside the steel cylinder is covered by a 10 cm thick CH₂ layer with a 10cm diameter hole in the center for the muon stopping target monitor pipe.

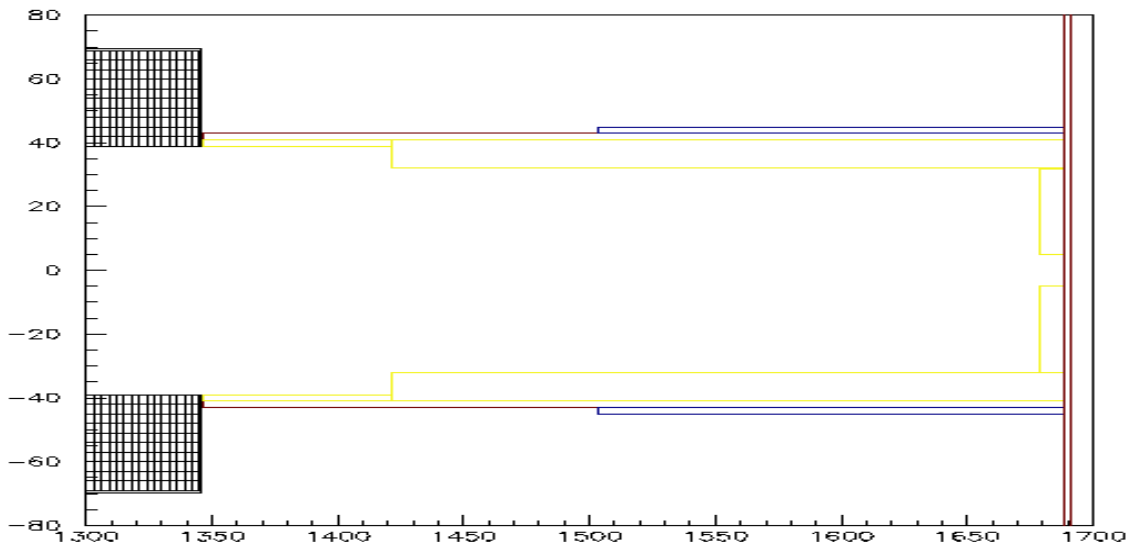


Figure 1.8 Beam stop design showing CH₂ (yellow), stainless steel (red), Lead (blue), and the calorimeter (black cross-hatched).

The chosen design of the beam stop not only largely suppresses the contribution to the rates from secondary interactions in the beam stop region, but also leaves enough room for cables in the vacuum volume outside of the beam stop.

1.7 Detector Support Structure

1.7.1 Introduction, Choices and Constraints

In this section we discuss the mechanical support structure for MECO elements in the Detector Solenoid. These are the muon target and its thin proton shield extension, the tracking detector, and the trigger calorimeter. For discussing its support structure, we treat the muon beam stop as another “detector”. Not part of the detector support, but interacting closely with it is the rear vacuum endcap that closes the vacuum volume. Also interacting is the back end of the cosmic ray shield (CRS), and the muon target monitor.

We constrain the detector support structure by several choices:

- All initial detector assembly, subsequent service, repairs, or element replacements are done outside the solenoid.
- All electrical cabling and gas or fluid plumbing are completed outside the detector, including the inside connections to the vacuum feedthroughs into the solenoid. This allows complete electrical testing of the cabling and integrity testing of all gas and fluid lines, as well as the commissioning of the entire detector system before its insertion into the solenoid.
- An absolute stay clear radius for conversion electron trajectories.
- No articulation of cabling and gas lines inside the solenoid. It would violate the stay- clear constraint.
- Maximal rigidity of the support structure for each detector to preserve relative location of the detector elements. Ideally, the rigidity should be at level of detector resolution for the tracker. This internal rigidity requirement for each detector is not imposed for the relation between the beam stop, the tracking detector and the calorimeter.

To satisfy these constraints, a rail and cart system is used to roll the detectors into and out of the solenoid through the downstream end after the bolt circle of the vacuum flange is undone. For the no-articulation and connections-outside constraints, all the vacuum feedthroughs are on the instrumentation feed-through bulkhead (IFB). The detectors roll forward or backward together with the IFB, so that cables and gas lines with nominal slack stay connected during the move. The two detectors are mounted on separate carts to keep the cart length shorter, helping the rigidity constraints. The two detector carts and the IFB are coupled together with fixed-length couplers. A third cart, for the muon target and proton shield, is rolled into the solenoid independently, not coupled to the others. It can stay in place when detectors are rolled out for servicing. In addition to instrumentation feed-throughs, the IFB also provides easy access to the Muon Beam Stop (MBS). This is accomplished through an access cover on the end face of the IFB. The cover also contains a 10 cm. diameter window on the beam axis for the x-ray monitor of the muon target.

1.7.2 Rails and Roll-in Sequence

Three separate track systems are needed in moving the detector-MBS train and the rear closure of the cosmic ray shield.

A rail pair is mounted directly to the inside wall of the solenoid for supporting and moving the three internal carts. These rails will be precision, track and ball-bearing roller systems for reproducible positioning of the detector and target carts. The internal rails end just upstream of the MBS, but are extended rearward on a series of vertical stand-offs during the installation.

The heavy 2.0 m long MBS rolls on its own rails mounted on the on top (inside) of the 0.5 m thick iron magnet return yoke which also serves as part of the passive cosmic ray shield. The bottom quarter of this yoke stays in place, supporting the MBS rail. The lateral positioning needs to be only accurate enough to align the IFB flange bolt circle. These rails can be made with conventional railroad type track and flanged wheels. These rails also get extended on vertical stand-offs during the installation.

Finally, a heavy duty pair of rails on the AGS floor is used to roll back, by about 10 m, the transverse cosmic ray shield (CRS) of 0.5 m of iron or stainless steel, scintillators and concrete. A 2 m section of the top 3/4 of the magnet return yoke is cantilevered from the transverse and rolls out with it to give access to the bolt circle of the IFB flange.

Figure 1.9 and Figure 1.10 show the steps in the installation sequence. The installation starts with the cosmic ray shield in its rear open position, the MBS in its backmost position, and all track extensions in place. The muon target cart and the two detector carts, with the tracker and calorimeter already mounted, are in turn lifted onto the detector rails. The couplings connecting the MBS and the detector carts are installed. All wiring and gas lines are installed and fully tested. At this point the installation is stopped for the complete commissioning of the detector system.

Because the outside rails accommodate the entire muon target and detector system, the detector commissioning can be done before, or in parallel with, the installation and testing of the superconducting solenoids.

After the solenoid is ready and the commissioning is completed, the detector-MBS train is rolled forward, with the rail extensions removed one by one: first for the detector rails, then for the MBS rails as their respective carts move them.

When the detector carts are in place, the IFB flange is bolted. The final step is the forward rolling of CRS to complete the enclosure just behind the muon beam stop. The muon monitor pipe travels with the CRS and is not physically coupled to the thin window in the IFB. The entire procedure is reversed, step by step, during a roll-out for servicing.

Table 1.5: Detector solenoid inner radial constraints.

Name	Dimension
DS cryostat inner radius	0.95m
Stay clear radius	0.68m
Tracker outer radius	0.70m
Typical detector inner radius	0.38m
Thickness of Proton absorber	0.03m
Clearance	0.03m

1.7.3 Radial Dimensions

The detector supports must satisfy a set of radial limits enumerated in Table 1.5. The radial space between 0.68 m and 0.95 m is shared by the polyethylene neutron shield, tracks, the detector support carts and structures and the entire cable plant for the detectors, all gas and fluid lines, on-board electronics, and clearance space. Coexistence is at a premium.

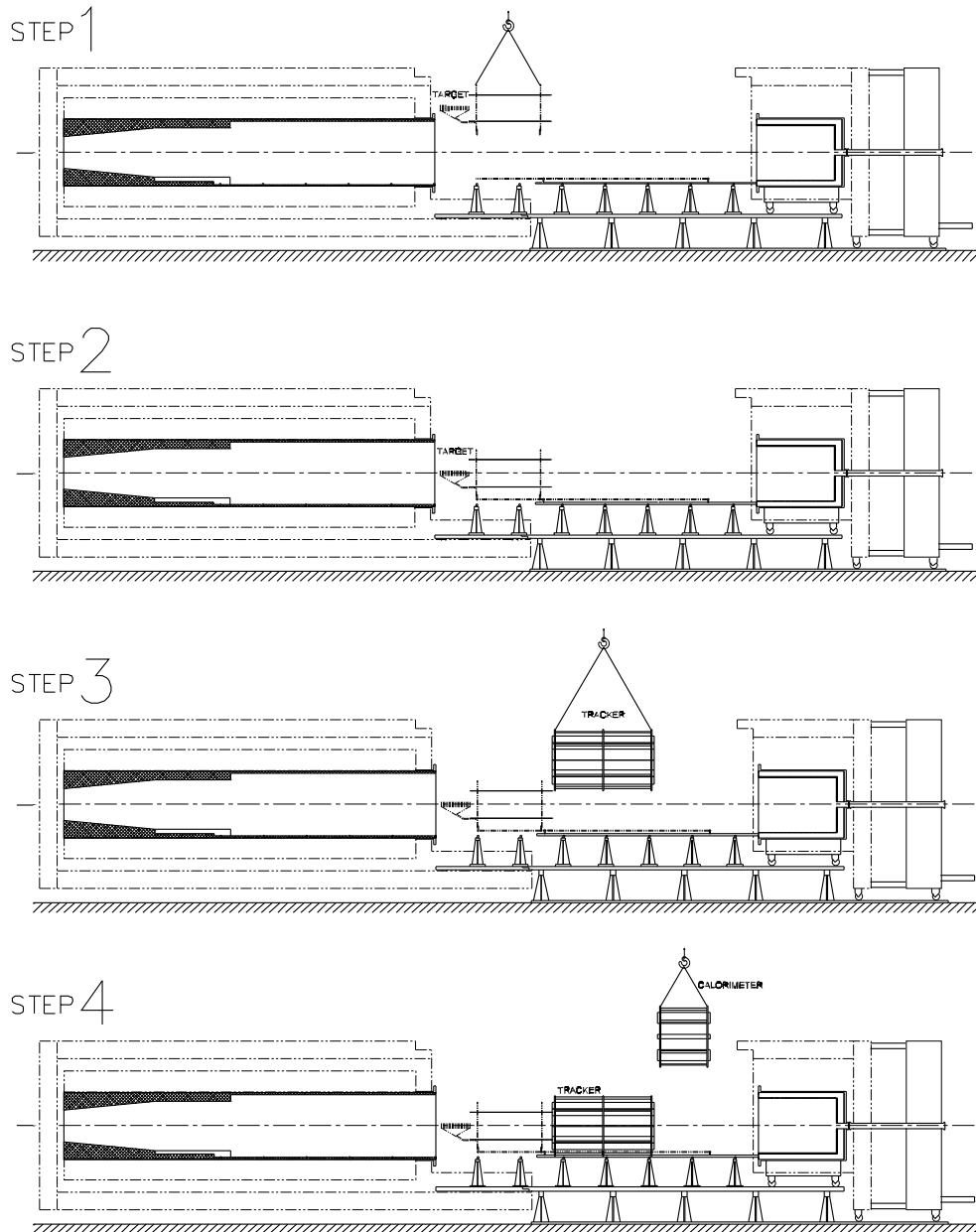
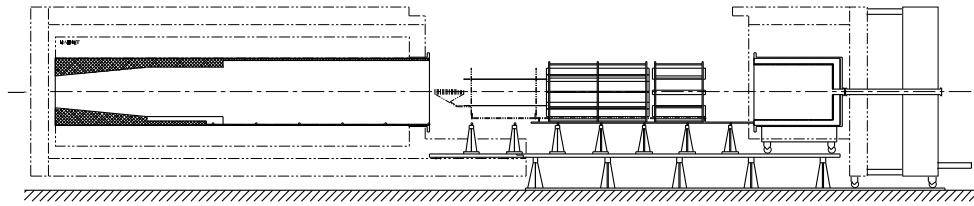
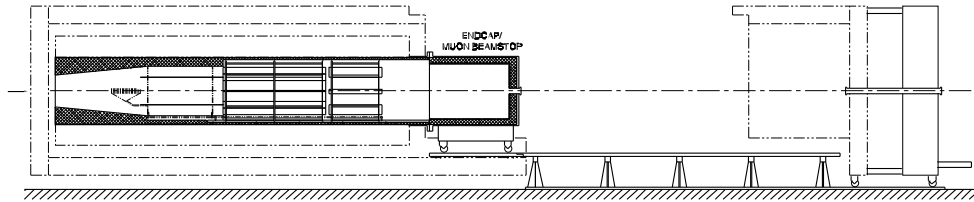


Figure 1.9: Steps 1 through 4 starting the Installation Sequence. The muon target, detectors, and muon beam stop in this installation drawing are from earlier designs; however, the overall scale is still appropriate.

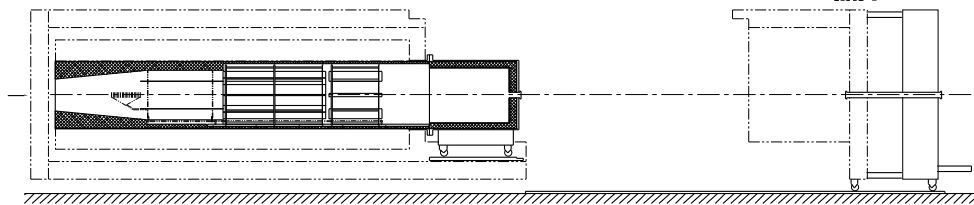
STEP 5



STEP 6



STEP 7



STEP 8

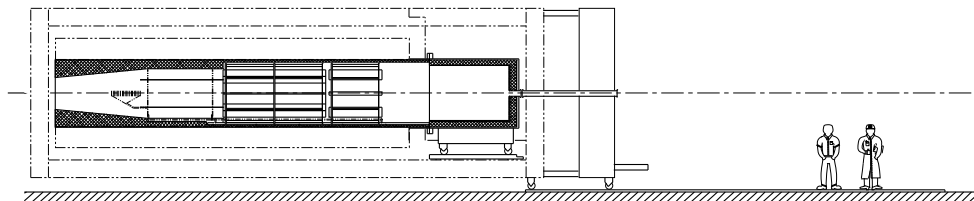


Figure 1.10: Steps 5 through 8 concluding the Installation Sequence.

1.7.4 Detector Cages and Carts

The support structure is similar for all three carts: a rigid rib-and-truss cage surrounding the detectors and riding on the rollers.

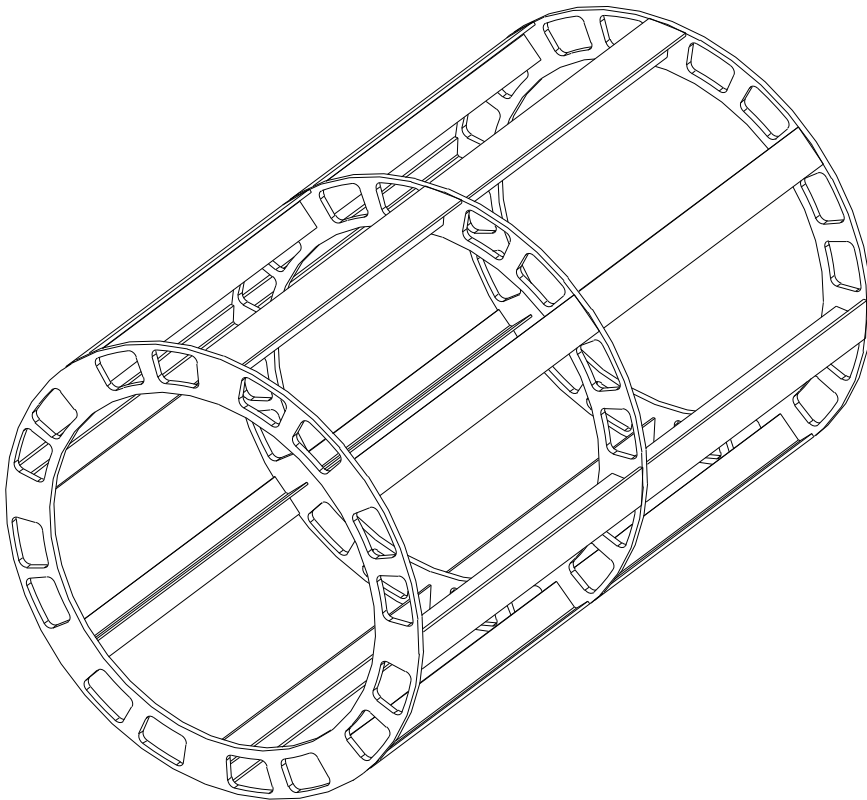


Figure 1.11: Isometric Drawing of a 3-rib detector cage.

The basic structural element is a transverse rib: an Aluminum annular disk with inner radius at the stay-clear and largest practical outer radius. Large holes, cut in the ribs all around the circumference, provide a path for cables and lines without compromising their mechanical integrity. The total cross-sectional area available in the cable penetrations is 3700 cm^2 . The cage construction is shown in Figure 1.11.

Consecutive transverse ribs are connected by longitudinal Aluminum trusses, made from bisected I-beams, to form a rigid cage. Details such as the number and thickness of ribs and the length of connecting trusses will vary detector by detector, but the elements are the same. The detectors are mounted directly to the cage. Figure 1.12 shows a cross-section of the tracker cage and detector; Figure 1.13 shows the same for the calorimeter cage.

The internal rail system will either be stationary rails with moving rollers or moving rails on stationary rollers; the choice will be made as part of the detailed design.

The polyethylene neutron shield at the outer radius, 3-5 cm thickness in the detector region, will be mounted directly on the solenoid wall. Therefore, the rib extends from the 0.68 m stay-clear radius to 0.88 m, giving a width of 0.2 m for the rib annulus. The rigidity of the cages will be calculated in a finite element analysis as part of an engineering design.

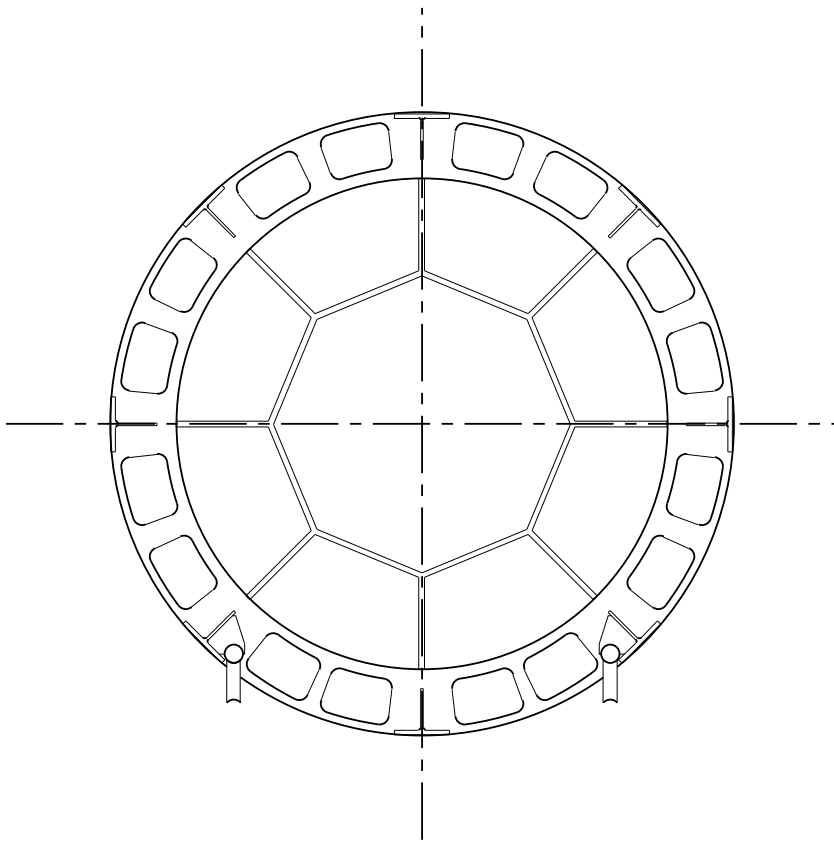


Figure 1.12: Cross Section of Tracker Cage with the Longitudinal Tracker Detector.

For the tracker, the length of the cage is 3-3.5 m and the detector weight supported is negligible. The cage provides a convenient mounting platform for the tracker. The tracker cage length will exceed the tracker length for diagonal tensioning of the tracker straws, as is needed. The mounting, complicated by the need for load transfers during the installation and the evacuation of the vessel, will be done in the detailed engineering design. The calorimeter cage, 1.5 m long, supports 4 individual detector vanes each weighing 600 kg, for a total of 2.4 tons. For the target/absorber cart the weight supported is entirely negligible, but the length is about 3.35 m. Each detector cart rides on a three point support, with two rollers on one rail and one on the other, to avoid torques on the cages. The single roller will have some sideways freedom for rail spacing tolerance.

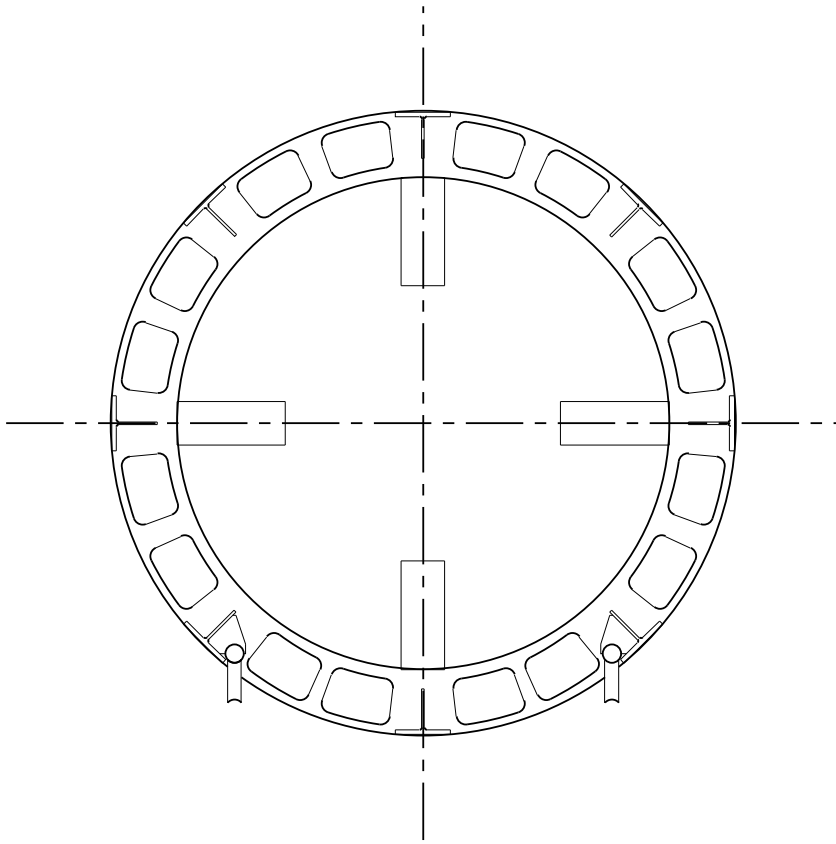


Figure 1.13: Cross Section of Calorimeter Cage with the Calorimeter Detector.

1.7.5 Surveying

It will be practical to put several survey targets on the detectors and cages, to determine the position of calorimeter and tracker, and check for deformations of the cages, by doing a laser instrument survey of the targets after the detector has been rolled into place and is under vacuum. The 0.4 m inner clear radius of the detectors provides a line of sight to survey the stopping target disks from downstream. We will have three small glass sight windows in the muon beam stop, to allow this survey. The element-by-element alignment and survey of each detector, on the other hand, is only practical while the detectors are outside the solenoid.

The usual technique of using a beam with straight-line particles to do a final survey adjustment is not practical; when the DS is off, a beam transported through the TS will blow up on exit. Cosmic rays at 45° will be a partial answer. Helical particle tracks in a reduced magnetic field, will be used to calculate any effective offsets from the surveyed element positions, but the interpretation will be more complicated than for a straight track.

1.8 Vacuum System

Vacuum is required in the detector solenoid mainly to limit backgrounds from muons stopping on gas atoms, followed by either muon decay or capture. The DIO endpoint (also the μ -e conversion electron energy) is given in Table 6 for different elements {Shanker:1982}. As discussed earlier, the DIO process is a steeply falling background with an endpoint energy given when the two neutrinos have zero energy.

The muon mass is $105.66 \text{ MeV}/c^2$. Nuclear recoil reduces the energy for light nuclei and the Coulomb binding energy reduces it for heavy nuclei. The end point for Aluminum is 104.96 MeV . Oxygen, present in the residual gas from small air leaks, and Fluorine, present in the residual gas from tracker gas CF_4 leaks, have the highest DIO endpoint, 105.1 MeV . The difference between these endpoints and the Aluminum endpoint, 0.14 MeV , is not significant compared to the detector resolution. Therefore, for the Aluminum target, the gas does not introduce a “physics” background, and only contributes to the overall detector rates. These issues still have to be studied for a Titanium target, including low Z impurities in the target itself. Our estimate shows a detector solenoid vacuum pressure of 10^{-3} Torr should be adequate for the Aluminum target {meco139}.

Table 6 Maximum electron energy for different elements.

Element	Z	E_{max} (MeV)
H	1	100.29
He	2	104.19
Li	3	104.78
Be	4	104.95
B	5	105.04
C	6	105.06
N	7	105.09
O	8	105.10
F	9	105.11
Ne	10	105.08
Na	11	105.06
Mg	12	105.01
Al	13	104.96
Ti	22	104.30

The ability to withstand high voltage discharge in a gas is a function of the pressure {Vonengel}. The minimum voltage difference without gaseous discharge for Nitrogen is only 275 V . This occurs when the distance d and pressure p satisfies $pd = 0.75 \text{ Torr-cm}$. This is called the Townsend limit, and occurs when the energy acquired between gaseous collisions is greater than the ionization potential, and the number of collisions is sufficient to initiate a gaseous discharge. At lower voltages, a spark will not occur, but a glow discharge will develop. For our geometry, a gas pressure of 10^{-3} Torr is adequate for the detector high voltage {meco 139}.

Scattering of beam particles into the detector acceptance in 10^{-3} Torr vacuum was evaluated and found to contribute negligibly to the detector rates. The multiple scattering and energy loss of the conversion electrons contributes negligibly to the signal resolution at 10^{-3} Torr .

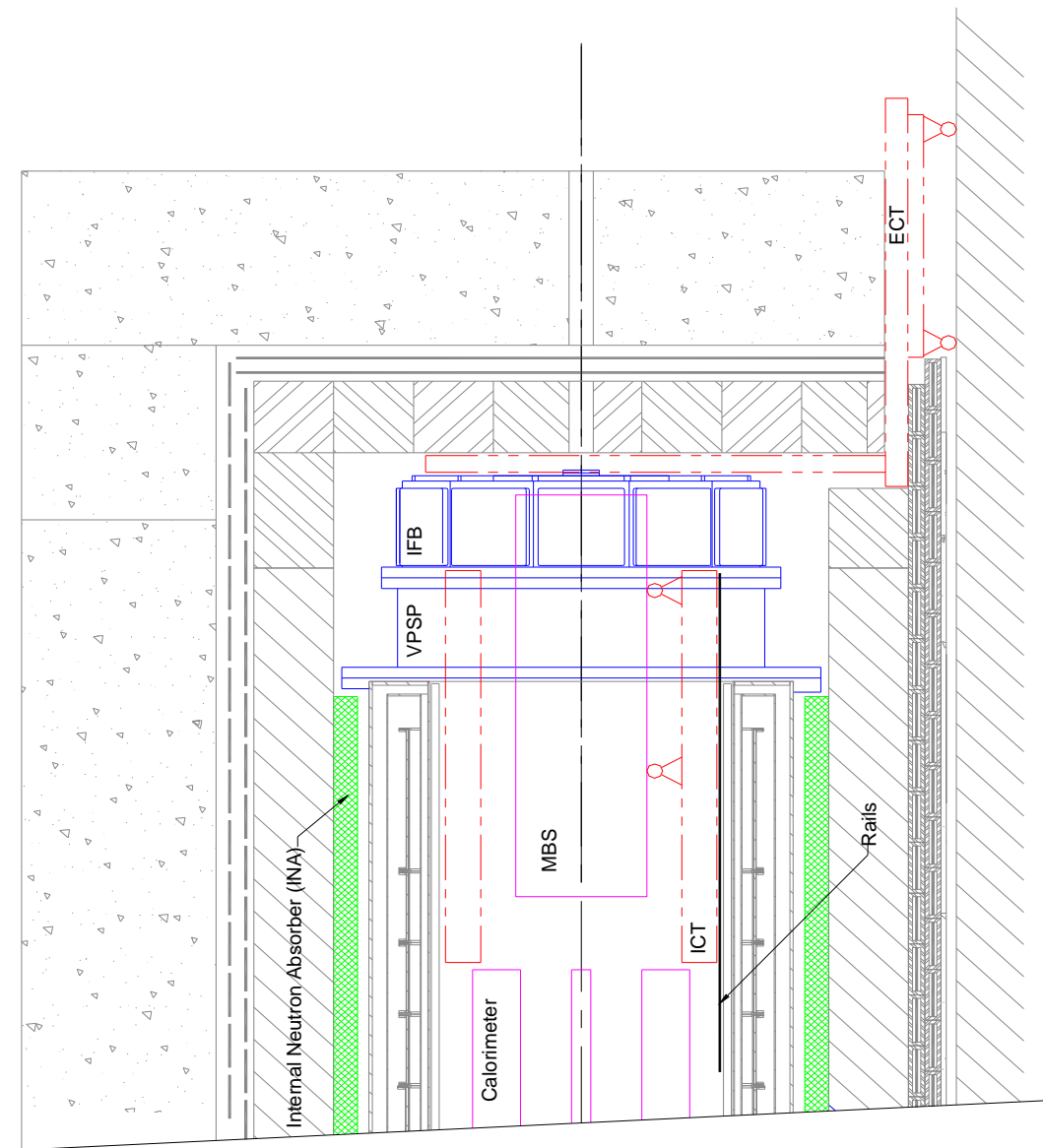


Figure 1.14 DS Vacuum Closure Elements. The muon beam stop in this drawing is from an earlier design; however, the overall scale is still appropriate.

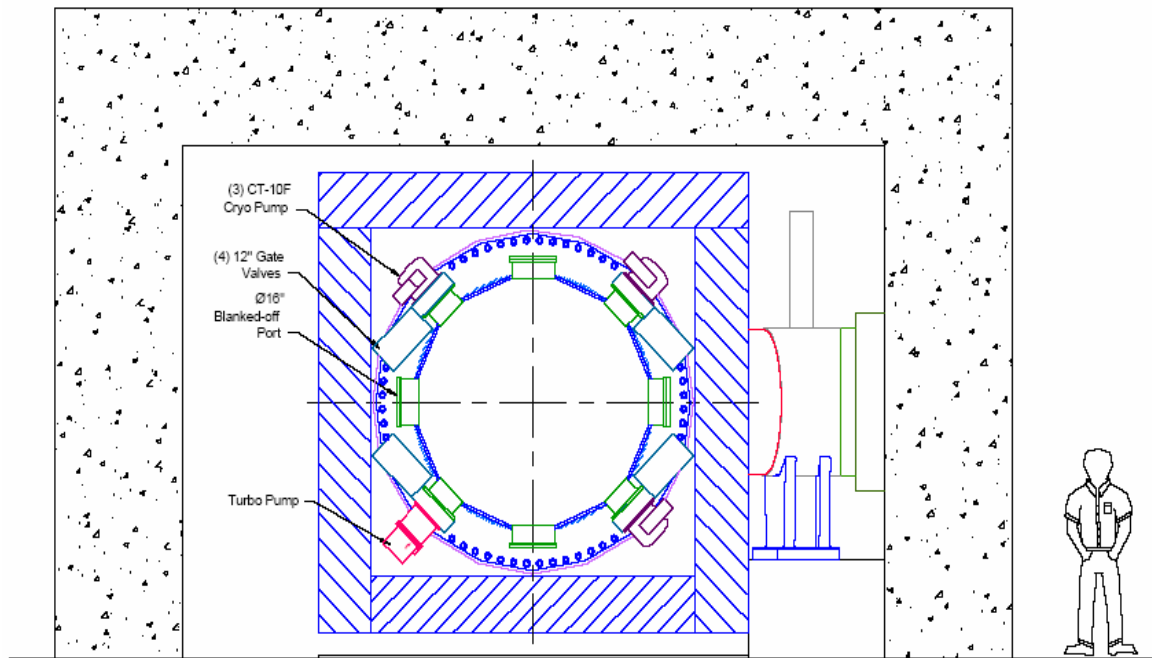


Figure 1.15 showing the three cryo vacuum pumps, one turbo pump, and four spare ports.

The Detector Solenoid requires a closure at its downstream end to:

- Close off the vacuum space of the magnet warm bore.
- Provide a connection and mounting place for the pumps used to generate and maintain the warm bore vacuum.
- Provide instrument, power, gas and cooling feed-throughs to bring these lines through the vacuum barrier.
- Provide for the orderly routing of cables.
- Provide partial mounting and support for the Muon Beam Stop (MBS).

As the design of the vacuum closure evolved, it became apparent that the best way to satisfy the design requirements was to do so with separate elements which worked together. The vacuum closure is made up of the following four elements:

1. Vacuum Pump Spool Piece (VPSP)
2. Instrumentation Feed-thru Bulkhead (IFB)
3. Internal Cable Tray & MBS support (ICT)
4. External Cable Tray Cart (ECT)

This is illustrated in Figure 1.14. The vacuum pumps mounted on the VPSP are shown in Figure 1.15. The three CF-10 cryopumps {meco130} have a total effective pumping speed of 6×10^3 l/s for air, 4×10^3 l/s for CF_4 , and 5×10^3 l/s for C_4H_{10} . The latter two are suggested tracker gases. With three cryopumps, we can isolate one for maintenance or regeneration while maintaining the DS vacuum with the other two cryopumps. The pump-down of the 2.5×10^4 l DS volume begins with a SDV-320 dry screw pump located outside the shielding. When the pressure drops below about 0.5 Torr, the gate valve to the SM141001 turbopump is opened. When the pressure drops below about 0.01 Torr, the gate valves to the cryopumps are opened. The turbo-pump must be shut down before the magnet is energized, as the

fringe magnetic fields are above the pump specifications. The DS pressure vs. time during this initial pump-down phase is shown in Figure 1.16. The magnetic field specification for the cryopump is $B < 0.12\text{T}$. The fringe field at the location of the cryopump is 0.11T . A study by C. Chen of the UCI group showed that with simple magnetic shielding of three 5cm thick iron plates, the fringe field at the cryopump could be reduced to 0.5T with an acceptable influence on the DS main magnetic field {meco130}. The physics/engineering optimization will be performed when funds are available. The main radiation issue with cryo pumps is the Teflon coating on the cryopump displacers. Teflon degrades after a radiation dose of only 10^2 Gy . The vendor test data of the proposed rad hardened cryopumps showed no degradation in performance after $5 \times 10^5\text{ Gy}$. The calculated dose at the cryo pump location with the new MBS design {meco127} was only 12 Gy over the lifetime of the experiment (10^7s), giving many orders of magnitude safety factor.

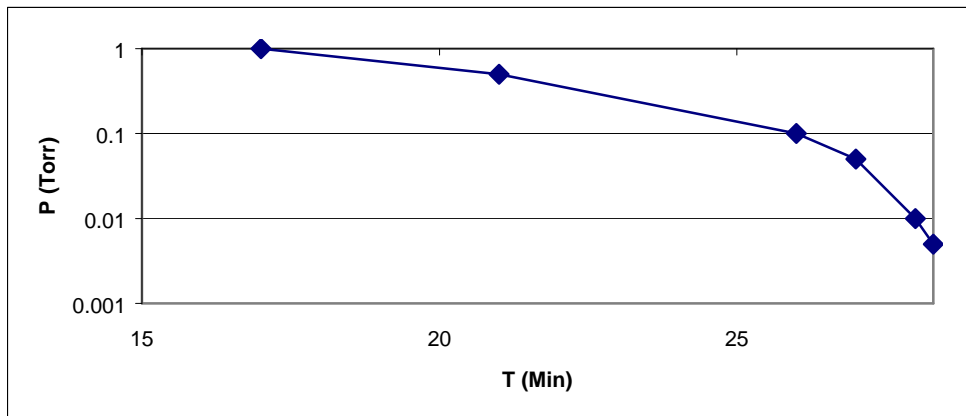


Figure 1.16 DS pressure during the initial pump-down. The cryopump gate valves are opened when the pressure is below 0.01 Torr.

The main gas loads are due to out-gassing of the shielding and beam stop materials, and leaks and gas diffusion from the tracker gas system. A calculation of the DS pressure vs. time after pump-down begins for the out-gassing vacuum load {meco130}, without bake-out, is shown in Figure 1.17. Our design goal is 10^{-4} Torr pressure after one day of pump down, so the present DS out-gassing load is acceptable without bakeout. This will be re-evaluated as the engineering design progresses. The straw leak rate extrapolating from the leak rates measured from single straws {meco119} is less than 0.1 Torr l/s . With two cryopumps, this gives a steady state DS vacuum pressure of $3 \times 10^{-5}\text{ Torr}$. Although the physics requirement is 10^{-3} Torr , we want to measure our detector rates, etc. as a function of gas pressure down to 10^{-4} Torr to verify our calculations, so the system design is adequate even if the tracker system gas load is three times greater than our extrapolation using the single straw leak rate measurements. Since the engineers have learned to be skeptical of physicist's extrapolations, they added four spare ports. Our vacuum system design will be re-evaluated after the tracker system gas load has been measured.

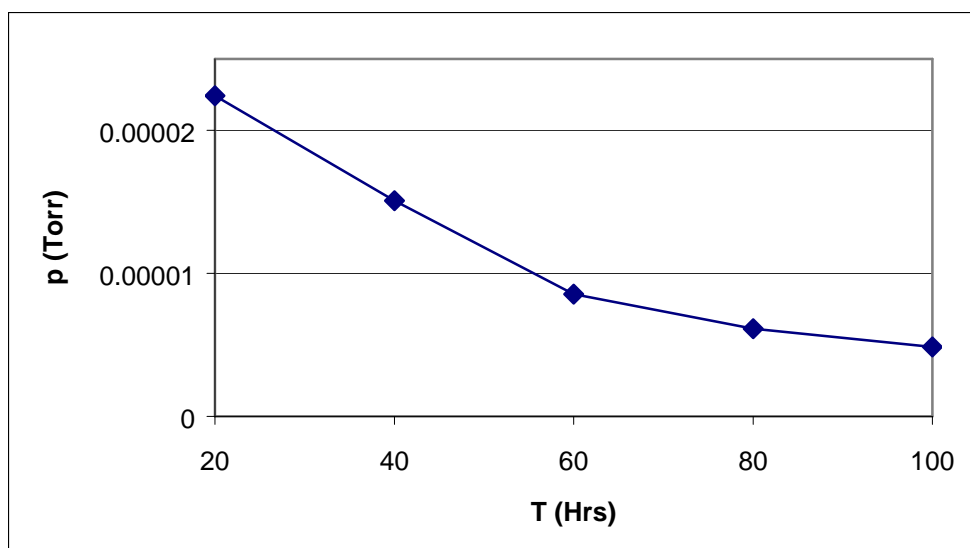
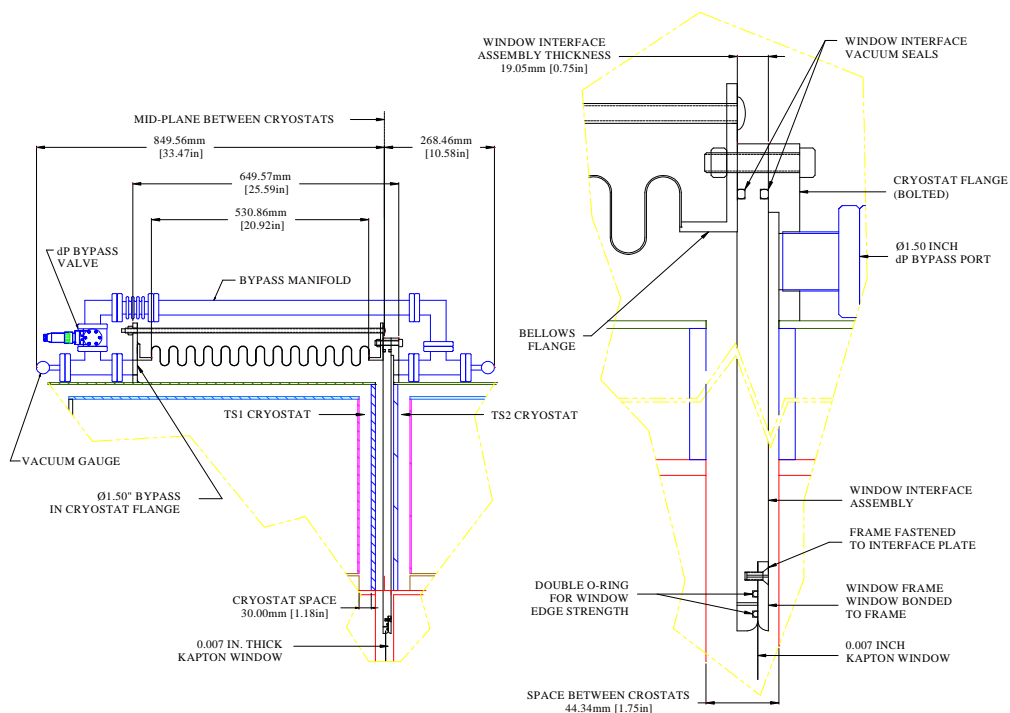


Figure 1.17 Calculation of the DS pressure vs. time after pump-down begins for the out-gassing vacuum load only.

The .007 inch thick Kapton anti-proton stopping window (see Figure 1.18) also serves to separate the DS and PS vacuum spaces (see MECO Reference Design). This is necessary to prevent neutral radioactive atoms from diffusing into the detector region. The PS vacuum system has not been designed yet; however, it should be much simpler due to the much smaller vacuum volume without detectors

Figure 1.18 Schematic drawing of the anti-proton stopping window assembly.



within it. The radiation dose to the anti-proton stopping window was estimated to be 12 Gy/s. Kapton degrades between 2×10^7 and 2×10^8 Gy. However, this window has vacuum on both sides, so the net force is nil during normal operation. It was calculated that the window will yield at 400 Torr pressure differential. Although it won't fail even at atmospheric pressure (760 Torr), it should be replaced if it

has yielded, since if it is stressed again from the opposite side at atmospheric pressure, it may fail. Probably the worst fault scenario is a water leak into the PS vacuum area. However, the saturated water vapor pressure at room temperature is only 30 Torr.

The pump-down procedure is first the PS-DS bypass valve will be opened and both the PS and DS will be pumped down. Once the pressure is well below 1 psia (50 Torr), the bypass valve will be closed. The vacuum control system will open the bypass valve if the pressure differential is greater 1 psia. After the first run, the window will be removed and tested to destruction to verify our radiation dose degradation calculations, etc.

Figure 1.19 shows the vacuum instrumentation feed-through bulkhead (IFB) just downstream of the vacuum pumps. The IFB provides the DS vacuum closure and will be withdrawn together with the detector for maintenance between runs. The IFB provides the downstream termination of the internal cable tray. This design features modular, removable instrumentation feed-through panels. There are twelve facet covers, as seen in Figure 1.19, each with net area of 1935 cm^2 , and twelve wedge covers, as seen in Figure 1.20, each with an area of 1255 cm^2 . The calorimeter feed-through pin counts are given in Table 7. The last column shows the required IFB area. The calorimeter requires the largest number of vacuum feed-throughs, assuming the tracker digitizing electronics is inside the DS vacuum, and uses less than one half the IFB available area. Thus this is a very conservative design, assuming the tracker digitizing electronics is inside the DS vacuum

Table 7 Calorimeter IFB cabling.

Crystal count	1152	Area (cm^2)
Signal pins	4608	1162 - 3175
HV pins	2304	7200
Pre-amp power	216	300
Gating and Calib	144	4363
Gas Lines	8	800
Cooling	8	800
Thermo-sensors	576	397

Figure 1.19 Vacuum Closure Two-piece Configuration showing the VPSP with vacuum pumps and the IFB. The VPSP will remain attached to the solenoid while the IFB will be withdrawn during internal detector servicing.

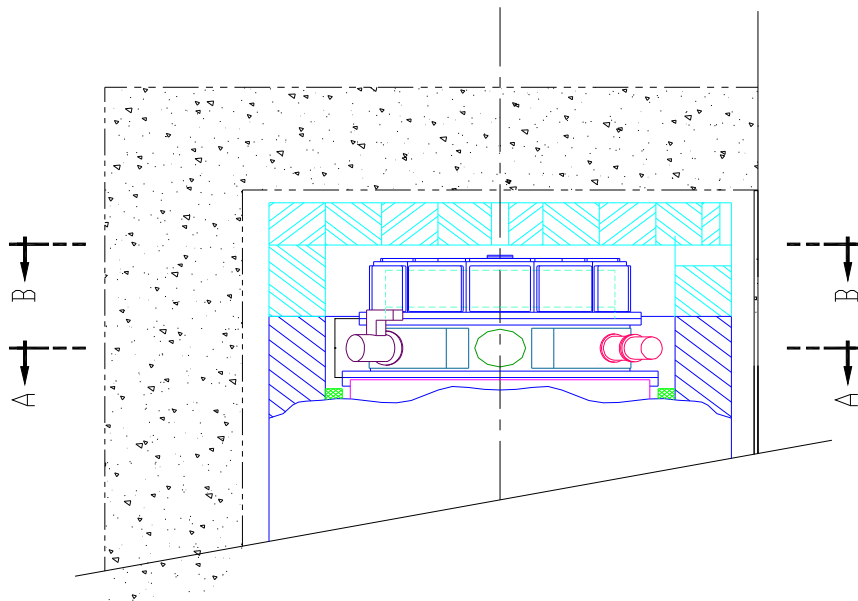


Figure 1.20 Perspective drawing of the IFB showing the facet covers and the wedge covers.

